High Temperature Method Of Measuring Electrical And Magnetic Properties Of Europium Doped Nickel Oxide

Seyedeh Parisa Torabi, B.Sc. Physics

Physics(Condensed Matter and Materials Science)

Submitted in partial fulfillment
of the requirements for the degree of

M.Sc. Physics

Faculty of Mathematics and Science, Brock University
St. Catharines, Ontario

Abstract

The measurement of the magnetic moment of materials as a function of temperature in modern AC or DC magnetometers normally has a limited high temperature range up to 400 K. To overcome this problem one needs to design ovens which can handle high temperatures. The highest Curie temperature observed in materials is in pure Co which is about 1400 K. However, most materials and compounds show T_c below 800 K. My thesis research topic is to study the substitution of Ni ions by rare earth ions in NiO. The NiO is a semiconductor which exhibits antiferromagnetism below 520 K, which makes it suitable for applications; to name a few, rechargeable batteries, and p-type transport conducting films. In this study, Ni ions were substituted by 2, 5, and 8 percent of Eu ions. The effect of substitution on the semiconducting properties of $Ni_{1-x}Eu_xO$ was studied as function of temperature from room temperature to 1000 K. To study the magnetic properties and the effect of Eu substitution on the Neel temperature of $Ni_{1-x}Eu_xO$ we adapted two ovens for high temperature measurements of AC susceptibility by using the ac modulation technique implementing a lock-in amplifier and the DC susceptibility using the SQUID magnetometer. To check the reliability of these two ovens we also examined the ferromagnetic transition temperatures of Bismuth Ferrite samples as function of Co substitutions for Fe.

Acknowledgements

I would like to express my deepest appreciation to my research supervisor Prof. Fereidoon S. Razavi for all the guidance and support He gave me and this thesis would not have been possible without his mentoring me through my master's degree.

I would also like to gratitude Prof. M. Reedyk and Prof. S. K. Bose for the valuable advice and comments throughout my graduate work as my committee members.

I must also thanks my parents for their unconditional love and support and my sisters for their encouragement.

I would also like to thank my boyfriend for being the source of motivation to me throughout this thesis.

I cannot begin to express my thanks to the electronic and machine shop, particularly to Stephen Renda and Gary M McDonnell for the great collaboration through my research work.

Many thanks to all my friends and colleagues, in specific Sara Hatefi Monfared for giving me strontium hexaferrite and bismuth feriite samples of her to be examined as test samples with the ovens and Mathew Pula for his helps.

Thank you to all the staff of Physics Department for their kindness and friendship specially Ivana Komljenovic Metcalf.

Contents

List of Tables

List of Figures

Chapter 1

Introduction

Nickel Oxide (NiO) is a transition metal oxide that exhibits antiferromagnetic (AFM) behaviour with a *Néel* temperature, T_N, of 523 K in bulk which is the highest transition temperature amongst transition metal oxides.[1] The NiO has a cubic crystal structure with a lattice parameter of $a = 4.189\text{A}^\circ$. Its energy gap E_g is about 4 eV, displaying semiconducting behaviour.[2]

Electrical properties in semiconductors, such as NiO are modified by doping an appropriate element. In this research, we have designed an apparatus for two different systems which will allow the study of magnetic and electrical properties of europium doped nickel oxide to high temperatures. Thus, this thesis presents the design of the oven and the application of the oven to our study of the structure, electronic, and magnetic properties of $Ni_{1-x}Eu_xO$ where x=0, 0.02, 0.05, 0.08 prepared by co-precipitation method.

Europium (Eu) is a part of the Lanthanide series with the electron configuration $4f^76s^2$ and has oxidation states of 2^+ and 3^+ with ionic radii of 1.17 A° and 1.12 A°, respectively.[3] The substitution of rare earth elements in NiO has been a topic of interest for years. [4] Whereby Eu has only recently captured scientific attention for showing the luminescent properties.[5, 6, 7]

To investigate the magnetic properties of NiO, we need systems capable of

measuring the magnetic properties to, at least, a temperature as high as 800 K. Our lab is equipped with a Superconducting Quantum Interference Device (SQUID) magnetometer for measuring magnetic properties of materials with a temperature limit of 400 K.

To overcome the temperature limit of the magnetometer, an oven has been designed and adopted for the magnetometer to reach a temperature as high as 800 K. In addition, I designed an AC magnetometer using a modulation technique capable of measuring the ac-susceptibility from 300 K to 1100 K. To check the reliability of the probes, I examined a sample of ferrite with a known Curie temperature (T_c) of 634 K.[8]

This thesis consists of the following chapters. In Chapter two I present a brief summary of how we can measure magnetic properties of materials using different methods. In chapter three I describe the design of an oven for the SQUID magnetometer system. Chapter four describes the design of modulation and pick-up coils for high temperature magnetic susceptibility measurement using a conventional oven for measurement between 300 K to 1100 K. This is followed by chapter 5 which presents the experimental results and discussion. In the conclusion, I suggest the needs for further improvement of the oven for the SQUID magnetometer as well as for the ac susceptibility system.

Chapter 2

Brief Theory and Measurement Techniques

2.1 Brief Theory

Considering electrons in a solid is different from considering electrons in an individual atom. In solids, atoms are positioned in a way to form the crystal structure. Depending on how the potentials of atoms overlap in the crystal, different types of materials are formed. Like electrons in atoms that have specific energy values and can be found in orbitals, in a crystal electrons can be found in energy bands and any other regions are forbidden to them. These energy bands are separated by forbidden regions known as an energy gap or band gap.[9] Depending on the value of energy gap in a crystal, compounds behave as metals, semiconductors, or insulators.

For alkali metals and noble metals with one electron per primitive unit cell the valence band is half-full. In general, metallic systems have partially filled valence bands, which can carry currents, i.e., in such cases the valence and conduction bands overlap. For systems where the crystal potential is weak, predictions based on free electron model are applicable.[9]

In semiconductors, the valence band is completely full while the conduction band is empty at absolute zero. As temperature increases, the electrons at the top of the

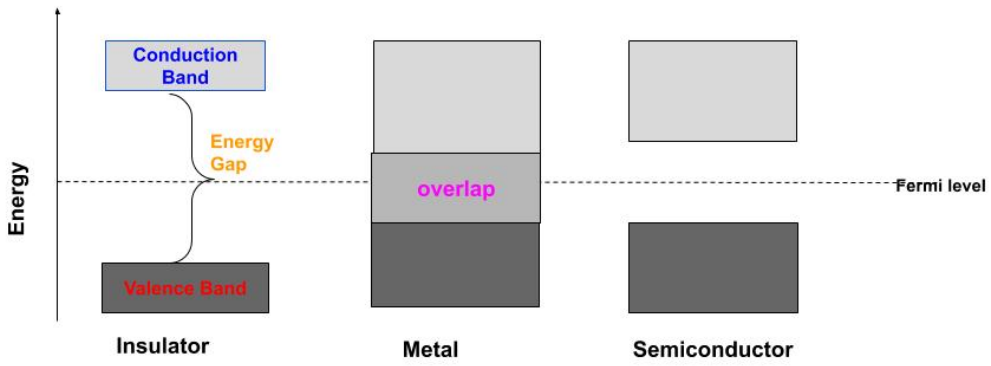

Figure 2.1: Schematic diagram illustrating the energy gap for insulators, metals and semiconductors. In metals the bands overlap and electrons easily move to conduction band. For semiconductors the energy gap is much smaller than for insulators.

valence band get excited and jump to the conduction band and leave holes behind in the valence band, In this case both electrons and holes can conduct electricity. As a result, the ratio of the energy gap to the thermal energy (E_g/K_BT) is less than 1 and the valence electron would become a conduction electron. Thus, semiconductors behave more like a conductor with increasing temperature. However, the energy gap in insulators is larger in value and thus with increasing temperature the ratio of the energy gap to the thermal energy remains bigger than one and the valence electrons can not leave the valence band hence no conduction.

2.2 X-Ray Measurement

Powder x-ray diffraction (PXRD) is a technique that is carried out on samples in order to confirm the crystal structure of the compound. PXRD is based on the Bragg law which indicates:

$$n\lambda = 2dsin\theta \tag{2.1}$$

where d is the distance between two successive layers in the crystal (lattice planes), Theta, θ, is the angle between the incident x-ray beam and the plane while n is an integer. Taking an elastic collision into account, the reflection angle of the crystal surface is the same as θ.

The Bragg law works out when two scattered waves interfere constructively and this condition is satisfied when the path difference between incident and reflected beam, $2dsin\theta$, is an integer multiple by the X-ray wave length, λ.

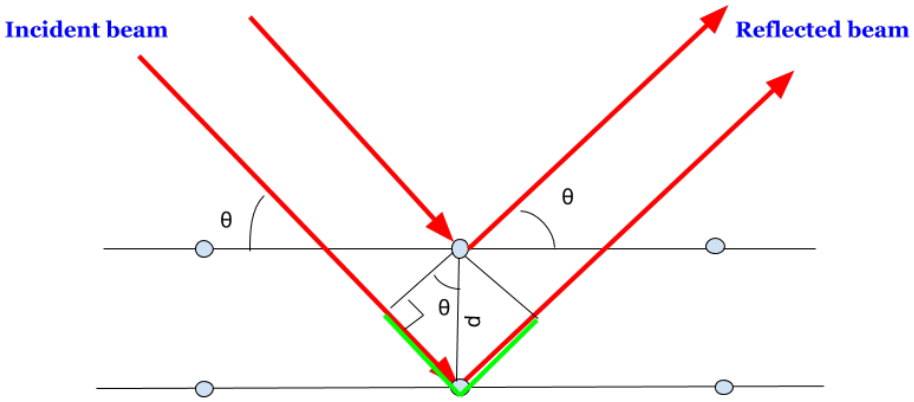

Figure 2.2: This figure shows the scattered photons of the x-ray within the crystal planes. θ is the angle between the incident/reflected photons, the green lines denote the path difference between the two beams which is equal to 2d$sin\theta$ where d is the distance between the planes.

PXRD thus can be used to detect different compounds by employing crystal structure characteristics and symmetry rules. Every crystal has its own diffraction pattern which is like a fingerprint of the compound.

2.3 Electrical Resistivity Measurement

The high temperature electrical resistivity of the samples was studied by an experimental set-up consisting of two quartz cylinders suspended by a spring. Two rectangular metal plates were used to contact the sample surfaces.

Two platinum wires were welded to each plate. The sample was placed between the plates and was held in position by tightening a spring loaded screw located at the top of the one end of the cylinder. After placing the sample properly between the plates, the sample probe was first placed in a quartz tube which was then placed in a tube furnace. Using a program written for the simulation mode of the Quantum Design software, Multivu, the measurements were carried out on each sample automatically.[10]
In addition, a temperature controller, a voltmeter, and a constant current of 10 nA were included in the set-up, where the sample resistance was measured using a four probe technique. By using Ohm's law, $V = IR$, a program was written in Delphi to measure the resistivity for the temperature range between 300 K and 700 K. [10]

2.4 Magnetism and Magnetic Measurement

Magnetism is the science of studying the response of materials to an applied magnetic field, H; the response is called the magnetic induction, B. Depending on the type of material the relationship between B and H varies. As an example, some materials indicate a linear dependency between H and B, However, in most cases, this relation is more complicated. In cgs, it can be written as:

$$B = H + 4\pi M \tag{2.2}$$

where M is called magnetization of the medium. The ratio of the total magnetic moment to unit volume, $M = m/V$ (emu/cm^3), determines the magnetization of a material which is a characteristics of the constituent ions, atoms or molecules. In addition, the total magnetization is a result of the interaction between dipole moments.[11] The magnetic induction in SI units is defined by $B = \mu_0(H + M)$ where μ_0 is called the permeability of the free space. The permeability (μ) is the ratio of the induced field to the applied field

that shows how permeable a material is under an applied field.

$$\mu = B/H \tag{2.3}$$

According to the equation 2.3, it can be concluded that the higher the induction, the more permeable the material is. Furthermore, another magnetic characteristic of a material is defined by the ratio of the magnetization to the magnetic field which is called the susceptibility, χ.

$$\chi = M/H \tag{2.4}$$

The magnetic induction B is equal to $B = \phi/A$, where ϕ is flux and A is area. As long as the flux inside the material is less than that outside, then the material is considered diamagnetic; however, if it is slightly more than that outside, the material can be either antiferromagnetic or paramagnetic. Furthermore, for materials where ϕ inside is much larger than outside, the material is either ferromagnetic or ferrimagnetic. If one considers the dipole moments of all of the constituent atoms and ions have a dipole moment then the total alignment of the moments under an applied magnetic field determines the type of material. Susceptibility and permeability both help to detect the characteristic behaviour of a material. They can be related by dividing equation 2.2 to applied field, the result in cgs is:

$$\mu = 1 + 4\pi\chi \tag{2.5}$$

and, the corresponding relation in SI would be:

$$\mu/\mu_0 = 1 + \chi \tag{2.6}$$

The susceptibility of the material provides information about the total alignment of the moments under the magnetic field. For instance, in paramagnetic regimes, the moments are randomly distributed in the material which by cooling down under a magnetic field

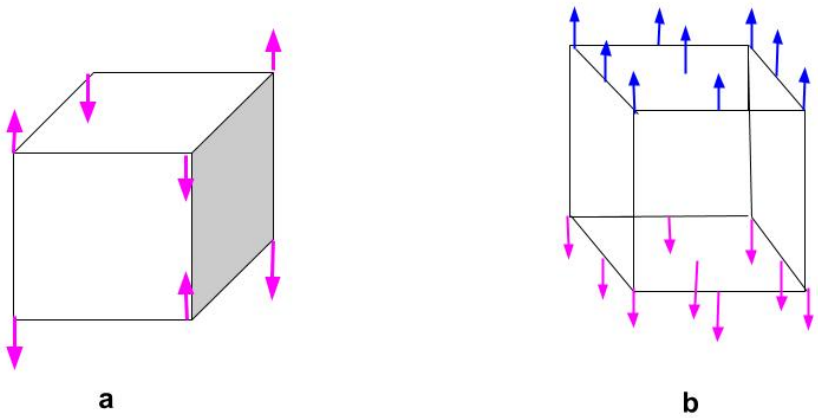

Figure 2.3: Schematic diagram of alignment of the moments a) shows the adjacent moments are aligned in opposite direction to each other in a cubic cell while b) shows the arrangement of moments in two sublattices of an antiferromagnetic.

can get aligned. In ferromagnetic materials, moments align in the same direction as the applied field and upon removing the field, there still remains a spontaneous magnetization.

There is also another type of material where moments under a magnetic field align in a way to keep the total magnetization zero. This is achieved either by alignment of the total magnetic moments of sublattices in opposite directions to adjacent sublattices or by having neighbouring moments align in opposite direction.

Magnetization is a function of temperature upon increasing the temperature the spontaneous magnetization, M_{sp}, goes to zero and the magnetic moments enter the paramagnetic order regime. In a paramagnetic state although M_{sp} is zero under the

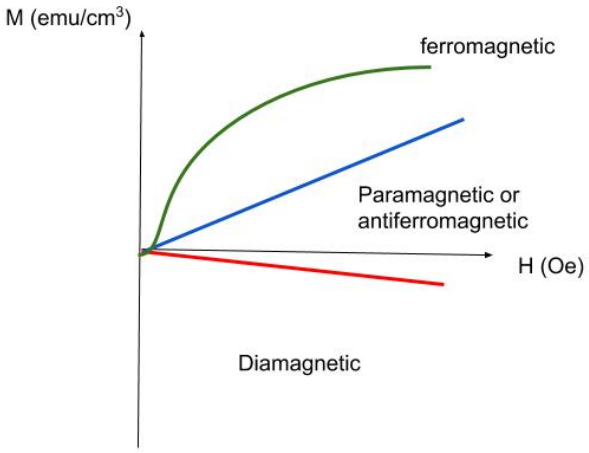

Figure 2.4: Schematic diagram showing the magnetization curves for the main types of magnetic materials. The slope of the graph gives the susceptibility.

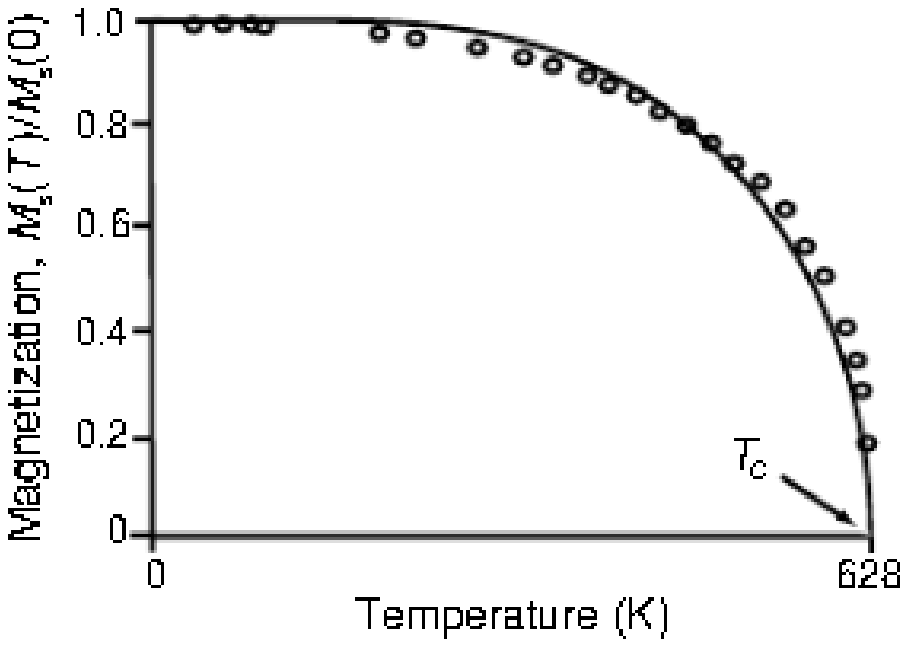

Figure 2.5: Temperature dependence of the spontaneous magnetization of nickel which goes to zero at T_c=628 K.
[9]

magnetic field, the atomic moments are aligned parallel to the field. This is the result of the magnetic induction which is caused by the permeability of the material. The temperature where ferromagnetic state collapses and the material becomes paramagnetic is called the Curie temperature T_c. Above T_c the susceptibility χ is no longer linear and follows the Curie-Weiss Law which is given by:

$$\chi = M/H = C/(T - T_c) \tag{2.7}$$

Where C is called Curie constant and T is the temperature. At the Curie temperature, T_c,the magnetic ordering is a continuous thermodynamic phase transition which comes from disordering of the dipole moments.[12] Additionally, at T_c the spontaneous magnetization falls to zero. This behaviour for nickel can be seen in Fig.2.3. The parallel

alignment is not the only possible arrangement of atomic moments. As mentioned earlier, in an antiferromagnetic material, atomic moments align antiparallel to each other. Assuming two anti-parallel sublattices where each lattice behaves like a ferromagnet then the total magnetization is zero. Indeed, the interaction between the moments in such a material, originates from an internal field, called the molecular field. Thus equation 2.7 can be generalized for both antiferroamgentism and ferromagnetism by rewriting it in a form of:

$$\chi = C/(T - \theta_{cw}) \tag{2.8}$$

where θ_{cw} is called Curie-Weiss temperature equaling to $C\lambda$ where λ is the proportionality constant between the average magnetic field (in the absence of an applied field) experienced by a magnetic atom and the magnetization of the system. Each magnetic atom is assumed to be sitting in a magnetic field created by all other atoms.[9] λ holds a positive value for ferromagntic order and is negative for antiferromagnetic order.[12]

This is a brief discussion of the structure, electronic and magnetic properties of materials. For a complete discussion on these properties, the reader is refereed to Solid State Physics by Charles Kittel [9] as well as Solid State Physics by Ashcroft and Mermin.[13]

As discussed earlier in the introduction, this thesis is dedicated to designing high temperature methods for measuring the magnetic properties of the materials which are discussed in detail in the following chapters.

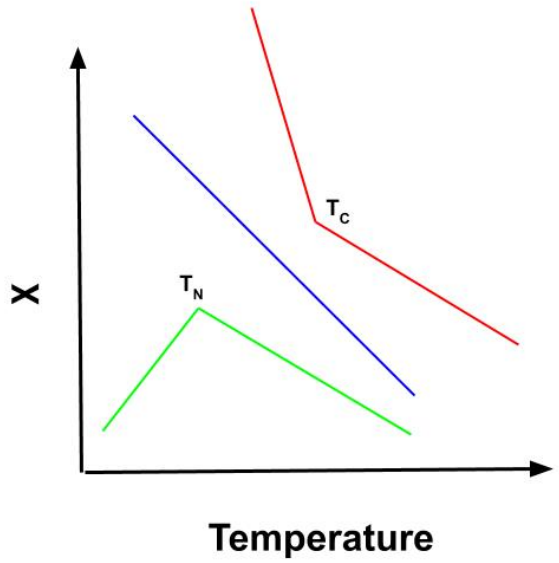

Figure 2.6: The temperature dependence of the susceptibility is illustrated. The green curve shows antiferromagnetism and the red one represents ferromagnetism. The blue curve which shows no transition is paramagnetism.

Chapter 3

The Design for an Oven Extension

To enable MPMS to go higher in temperature, an oven extension was designed. A new head block and sleeve were required to place the oven inside the Dewar.

This chapter discusses briefly the MPMS components followed by an explanation of the oven extension design.

3.1 Superconducting Components

The superconducting magnet provides a homogeneous DC magnetic field via a superconducting wire wrapped around a solenoid. Three pick up coils are co-axially located inside the magnet in a second-derivative order which means two are wound in the same direction (counter clockwise) while the third coil is placed at the center of the other two, wound in an opposite direction (clockwise), with a total number of turns equal to that of the other two, leading to rejection of the linear gradient of the external field. These coils are connected in series to the 4th coil near the SQUID detector (see Figure 3.1). [14]

Moving the sample inside the three coil assembly, causes magnetic flux changes in the 3-coil system which results in an induced current in the coil's circuit (Faraday 's law). This current induces a magnetic flux in the coil adjacent to the SQUID, which causes an induced ac-current (radio frequency) in the SQUID. [9] The pre-amplifier of

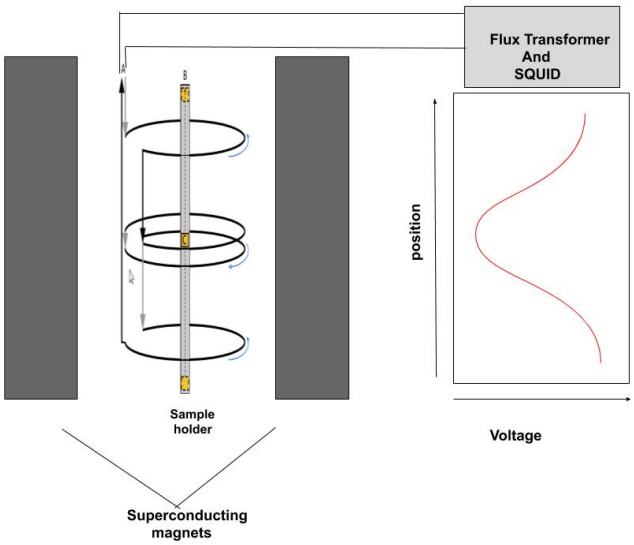

Figure 3.1: The reference position is illustrated.
[15]

the SQUID circuit then creates a voltage proportional to the ac-current which opposes the induced current in the SQUID (negative feed back). The induced voltage which is proportional to the magnetic moment of the sample in the pre-amplifier is detected by the system electronics and digitally transferred to the computer as the sample moves through the coil system in a step-wise process. The data points are read by the Multivu program[16], and the moment of the sample is calculated by fitting a curve to the data points. [17]

3.2 Sample Space And Heat System Control

The MPMS system has the ability to run the measurement up to 400 K.[18] To increase the temperature range of the measurement, a furnace attachment close to the sample was designed. Quantum Design used to provide a furnace extension before they discontinued the MPMS model. By comparing the original price of the oven and our design, it is a substantial saving to build one. Hence, a new sample space with a low magnetic

susceptibility and high heat transfer was designed. Brass as a non-magnetic material with a high melting point around 1500 K was chosen to be used as the sample holder.[19] In addition, new sleeves and a head block were made out of stainless steel to be equipped with the heater extension which is attached around the inner sleeve.

The sample space consisting of the head block and two sleeves was designed with a special type of double sealed to let the sample holder move through the sample space by the drive mechanism located outside of the chamber. Hence, the original sample space was replaced by a new sample holder including the furnace extension. The head block was mounted on top of the airlock with the standard O-Ring seals, and the sleeves were pushed inside the sample chamber of the MPMS system.

In addition, on the top of the head block a valve was designed to enable the user to evacuate, and purge the helium gas inside the sample space by pressing the air lock button of the MPMS system. To keep the sample space at low pressure the evacuate/purge cycle needs to be repeated twice. It has to be mentioned that the vacuum system was leak tested using a Helium leak detector. In addition, a turbopump was connected to the head block via the for mentioned valve. On the brass rod, a groove was cut to provide a space for the sample. To hold the sample on the sample rod, brass foil was used to wrap around the sample and the rod. This way, we can minimize the background magnetic moment. The diameter of the rod is 3mm (0.12") and the sample is located 20 mm below the detection coil system of the MPMS (see Figure 3.2).

To design the furnace extension, 6 ceramic tubes of 1.27 mm (0.05") diameter and 203.2 mm (8") length were used. In total, 1.22m (48") of the resistance wire, nichrome, was passed through the tubes and wound around the inner sleeve close to the sample to provide 100 Ω resistance for extending the temperature to 800 K. The resistance wire ends were connected to copper wires, which were pulled all the way up to the head block to connect to a temperature controller. The temperature controller provides

a maximum power of 50 VA (1 A at 50 V) allowing the experimenter to raise and stabilize the temperature. The magnetic moment versus temperature and field were obtained using a program written in Delphi5 employing the external device option (EDC) of the Multivu program of the MPMS system.

The temperature controller was calibrated manually and tested for the temperature range between 300 K to 800 K. To do so, a platinum resistance thermometer was inserted at the top of the ceramic rods which was calibrated by a thermocouple inserted in the inner tube at the center position of the sample space, the available space between the inner and outer sleeve which has a diameter of 0.55 mm (0.22"), close to the extension. The thermocouple voltage was read using a voltmeter while the platinum resistance voltage was read by the temperature controller. This way the read-out of the platinum thermometer was corrected during the measurement via a calibration factor written in the program running the measurement (see Figure 3.3). The calibration factor was obtained by plotting the temperature that was read by the platinum resistance versus the temperature that was read by the thermocouple which is shown in Figure 3.4.

The controller stabilizes the temperature and controls the rate of increasing and cooling down of the temperature by regulating the input current. To reach over, 800 K more input current was required which was made possible by adding a power supply to the output. The first few experiments were carried out manually to remove bugs and improve the system before running the measurement automatically. The new setup worked out successfully up to 750 K, however, we realize that our oven design produced too much heat above 700 K which affected the magnetometer cooling system above 700 K . To overcome this problem, we should minimize the length of the oven from 203.2 mm (8") to 127 mm (5") in order to reduce the radiation from the oven to the MPMS system, which is set at 230K during the oven usage, by about 30 to 40 percent (a factor of 5/8 approximately).

Figure 3.2: the head block and sleeves.

Figure 3.3: On the left the temperature controller is shown, as well as, a voltmeter(middle) to check the furnace temperature using a thermocouple. In front of the system the vacuum pump is seen which is connected to the head block on the MPMS.

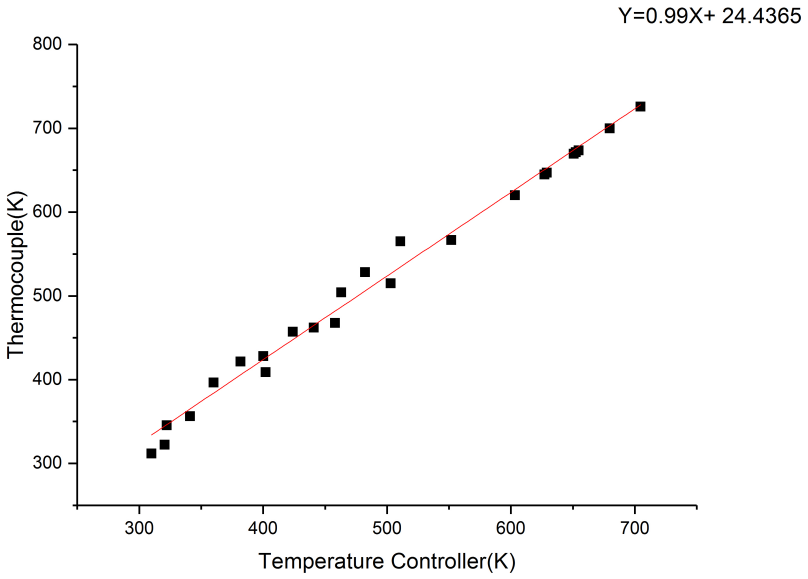

Figure 3.4: The platinum resistance thermometer temperature read by temperature controller versus the thermocouple temperature obtained from the voltage read by the voltmeter is plotted. The magnitude of the slope gives the accuracy which in this case is 0.01 per degree of kelvin.

Chapter 4

Modulation Coil Design

To study the AC susceptibility, the mutual inductance technique was used. Mutual inductance between two coils is the ratio of the penetration of the total magnetic flux, ϕ, into the cross-section area of the second coil as a result of a current, I, in the first coil which modulates the inner coil.[20]

$$M = \phi / I \tag{4.1}$$

Inductance arises from the circumferential magnetic field, B, caused by the current in a loop. This way, the magnetic field can penetrate the cross-section. In other words, having a coil that is wound with a number of wires very close to each other, without any connection in-between, all around the surface, produces a magnetic flux that can be obtained by taking an integral over the surface.[21]

$$\phi = \int_s B.ds \tag{4.2}$$

where the magnetic field B is surrounded by the wire coil with cross-section S. Taking the inductance method into account, two coils were built using the machinable ceramics. One as a modulation coil with a length of 75 mm (3”), having 150 turns of wires, and the other, as a sample holder with a length of 38.1 mm (1.5”) and 100 turns of wire wrapped around it. Moreover, the diameters of the first and second coils were chosen to

be 10.50 mm (0.41") and 6 mm (0.23") respectively. Furthermore, to prevent a connection between wires, the same number of grooves as the number of turns were cut on each coil. Figure 4.1 shows the grooves on the pick-up and the balance coil. In addition, Figure 4.2 schematically shows the grooves on the modulation coil, which is connected to the three tubes at the bottom.

To produce an AC magnetic field, the wire ends of the modulation coil were connected to the reference channel of a lock-in amplifier with a fixed frequency. The second coil that was placed inside the modulation coil comprises of two parts. One in which the sample was placed which is known as the pick-up coil and another known as the balance coil. Both parts were wound with the same number of turns of wire; 50 turns per half inch, in an opposite direction. This arrangement keeps the induced magnetic flux zero inside the inner coil. Hence, placing the sample inside the pick-up coil, will change the total flux which arises from the magnetization of the sample. The inner coil was connected to the input channel of the lock-in amplifier to detect the change in the total flux as an ac-voltage output due to the sample response under the applied ac-magnetic field. A voltmeter, a Keithley 2010 multi-meter, was connected to the lock-in amplifier to read its analogue output voltage proportional to the amplitude of the ac-voltage of the pick-up coil and transfer it digitally to the computer. Figure 4.3 shows this set up. The oven that carries the probe inside is shown, the lock-in (bottom) and the voltmeter (top) can be seen.

The ac-susceptibility versus temperature was obtained using a program written in Delphi5 employing the external device option (EDC) of the Multivu program of MPMS system.

The lock-in amplifier provides a time-dependent voltage V_o and a current I_o at a certain frequency, ω, which passes through the modulation coil via the output channel. Therefore, the voltage and the current can be calculated by:

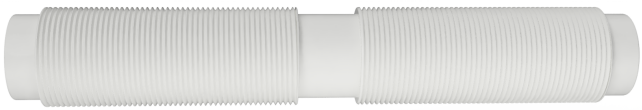

Figure 4.1: The pick-up and the balance coils before winding the wire.

Figure 4.2: The modulation coil.

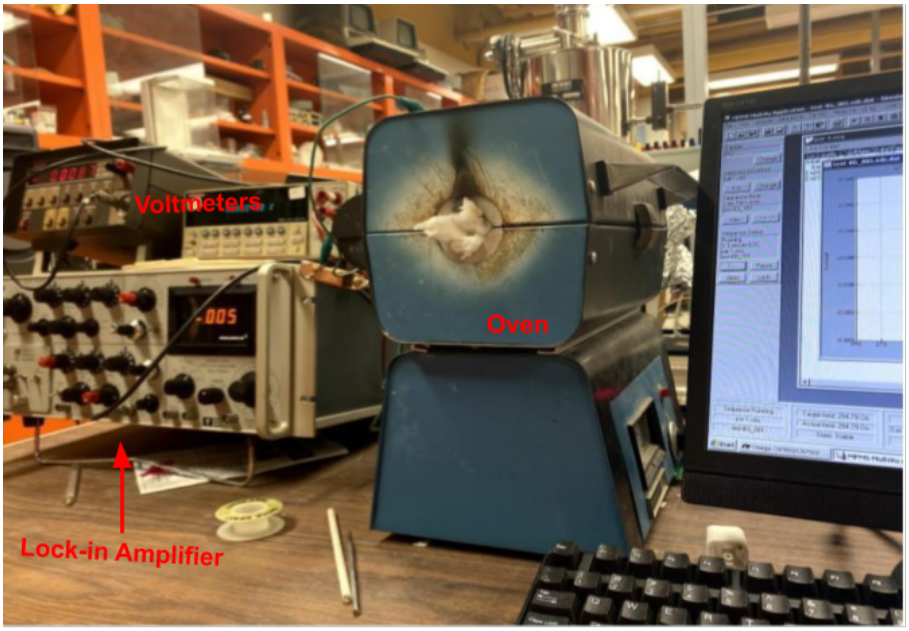

Figure 4.3: Modulation coil system.

$$V_mo = V_ocos(\omega t) \tag{4.3}$$

$$I_mo = I_ocos(\omega t + \delta) \tag{4.4}$$

where δ is the phase difference. Subsequently, a time-dependent field $\vec{H}$ is obtained by:

$$\vec{H(t)} = \vec{H}_ocos(\omega t + \delta) \tag{4.5}$$

In addition, the induced magnetization is proportional to the susceptibility and the magnetic field as $\vec{M} = X\vec{H}$. Thus, equation 4.5 can be presented as:

$$\vec{M} = \vec{M}_s + Re\vec{H}_oXexp[i(\omega t + \delta)] \tag{4.6}$$

Mathematically speaking, exp(i(wt+δ)) = cos(wt+δ) + i sin(ωt+δ), and by only taking

into account the real part of the multiplication of $\vec{H(t)}$ and X, equation 4.6 gets simplified to :

$$\vec{M(t)} = \vec{M_s} + X'\vec{H_o}cos(\omega t + \delta) - X''\vec{H_o}sin(\omega t + \delta) \tag{4.7}$$

By putting the sample in the pick-up coil, the total magnetic flux of the inner coil can be obtained by:

$$\phi_{inn} = \phi_p + \phi_b = \int_{A_p} \vec{B}ds_p + \int_{A_b} \vec{B}ds_b \tag{4.8}$$

where ϕ_p and ϕ_b are magnetic fluxes, and A_p and A_b are the cross-section areas of the pick-up coil and the balance coil respectively. Since the pick-up and the balance coils have the same dimension $A_p = A_b$ and by considering the relation between the magnetic field and Magnetization, $\vec{B} = \vec{H} + 4\pi\vec{M}$, equation 4.8 can be rearranged as :

$$\phi_{inn} = \int \vec{H}d\vec{s} + 4\pi \int \vec{M}d\vec{s} - \int \vec{H}d\vec{s} = C_1 + C_2(X'cos(\omega t + \delta) - X''sin(\omega t + \delta)) \tag{4.9}$$

where C_1 and C_2 are constants. Faraday's Law of induction can be written for a time-dependent magnetic flux as $V_{ind} = -Nd\phi/dt$ where V_{ind} is the induced voltage, N is the number of the turns and the minus sign denotes Lenz's Law which is expressing the induced current which is always in a direction to produce a magnetic field opposing the applied field.[22] As a result the induced voltage can be given by:

$$V_{ind} = -Cd\phi_s/dt = C^*(X'sin(\omega t + \delta)) + X''cos(\omega t + \delta)) \tag{4.10}$$

where C and C^* are constants. To read the sample temperature during the measurement, a type K thermocouple was used. A type K thermocouple consists of two wires, Chromel and Alumel which are joined together at one end, are called a junction(see Figure 4.4). The junction was placed on the top of the inner coil between the balance and the pick-up coil. The other ends of the thermocouple are connected to a voltmeter while the heater

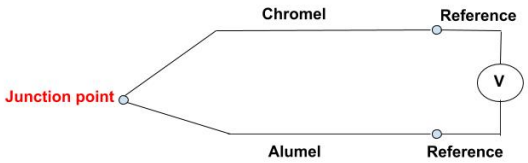

Figure 4.4: Schematically showing how k type thermocouple reads the temperature, the reference wires are associated with the voltmeter and are usually made of copper.

wires, including the probe inside of it, are connected to a temperature controller. The temperature controller itself is connected to the oven and is programmed by software on the computer. The reason for using a voltmeter is to connect to the type K thermocouple for taking advantage of the Seebeck effect to measure and read the sample temperature. The type K thermocouple has a measurement sensitivity or so-called Seebeck Coefficient (S) of 41 μV/°C with a full measurement range from -200°C to 1300°C.[23]

The other consideration in the design of the probe was to choose proper materials. Machinable Ceramics with a high-temperature tolerance were used for the coils. Also, to protect the wires from movement which could cause a short circuit, high-temperature fibreglass tape was used. In addition, non-magnetic and high-temperature tolerance wire was required to minimize the perturbation on the sample response. Chromite and copper are good candidates and chromite was selected since it showed less oxidation at higher temperature. Figure 4.5 shows the inner coil made using the chromite wire.

After winding the wires, their ends were pushed through three ceramic tubes(see figure 4.6). Each tube, includes two holes to prevent any connection between the wires, each dedicated to one pair of wire ends to connect them to the plug. One for the

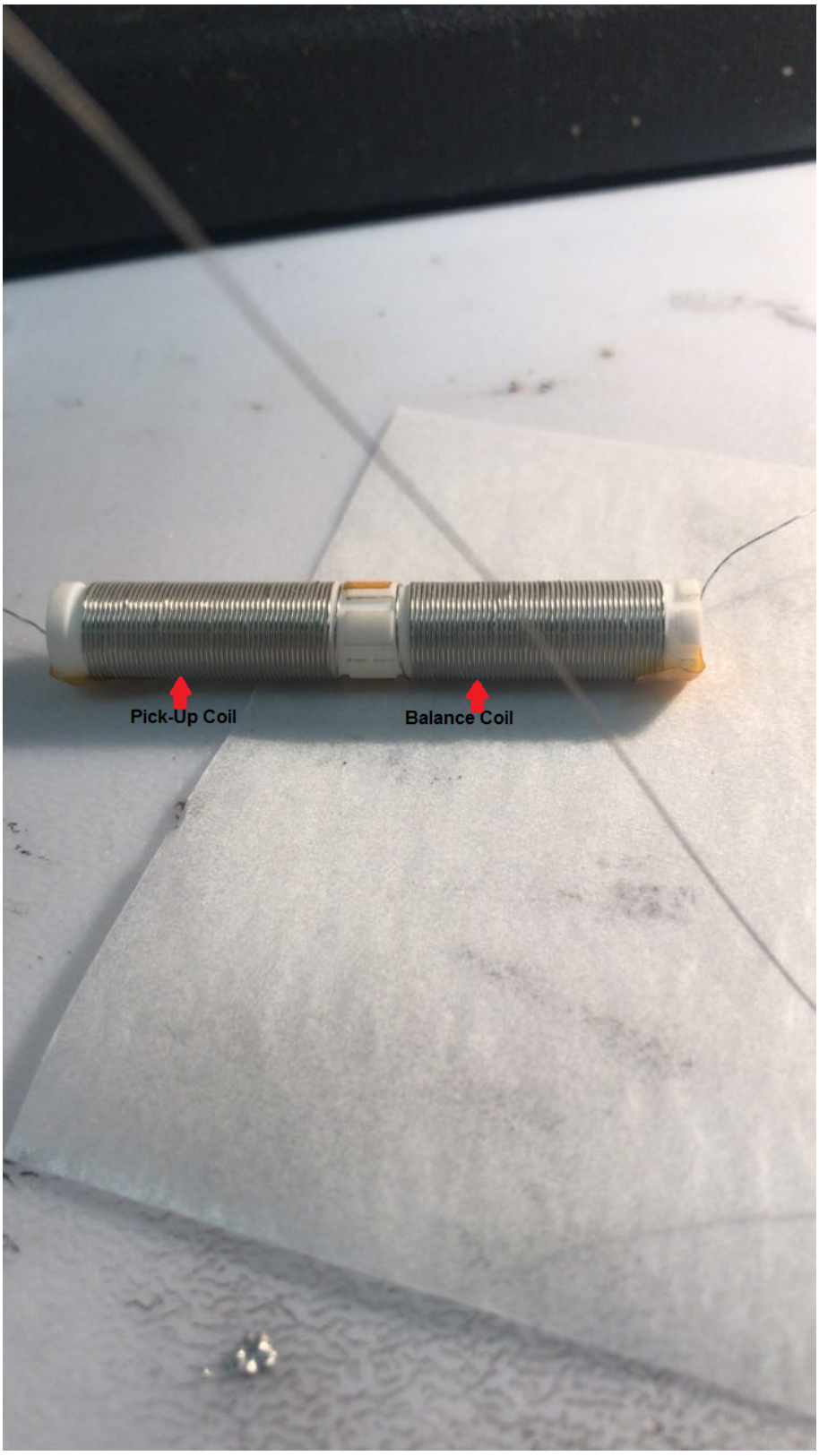

Figure 4.5: The Inner coil.

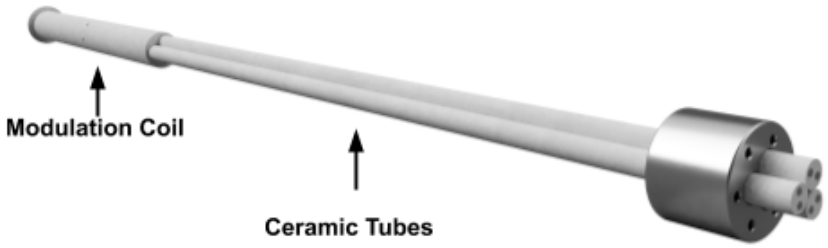

Figure 4.6: Schematically shows the three ceramic tubes which are attached to the end of the modulation coil by high temperature glue.

thermocouple, one for the modulation coil and one for the inner coil. Two coaxial cables were used for the coils, as well as a banana plug for connecting the voltmeter to the temperature controller.

Generally speaking, a lock-in amplifier is a device to detect very small AC signals in the range of nanovolts to millivolts. It uses a technique that is known as phase-sensitive detection(PSD) to measure and detect very small signals that are concealed by noise sources a thousand times larger. The PSD technique singles out the signal at a specific frequency and phase. This way, any other noise signals at different frequencies will be eliminated. The PSD technique enables the lock-in amplifier to detect the signal by decreasing the bandwidth to as narrow as 0.01 Hz which provides an accurate measurement.

To start the measurement, the modulation coil needs to be excited at a favourable frequency by an oscillator or function generator which is called the reference frequency, ω_r, and then the lock-in detects the response of the pick-up coil at that frequency. If the output from the generator is a sine function, the response signal can be a waveform.

Chapter 5

Results and Discussion

5.1 Sample Preparation

There are various methods for preparation of nanoscale particles which consist of three main classes including; the mechano-chemical method, the sol-gel method and the co-precipitation method. In this thesis $Ni_{1-x}Eu_xO$ samples were prepared using the co-precipitation method.

5.1.1 Co-Precipitation Method

To produce Eu doped NiO samples, the co-precipitation method was used. To prepare the pure sample, one molar nickel chloride hexa-hydrate, four molar sodium hydroxide and 0.1 molar ethylenediaminetetraacetic acid known as EDTA dissolved in distilled water as a dispersing solvent were used. The homogeneous solution obtained was stirred at room temperature while NaOH was added drop by drop until the pH value reached 12. Then the solution was heated at 60 C° for 2h while it was magnetically stirred. The same steps were used to produce the doped samples with using 2%, 5% and 8% of one molar europium chloride hexa-hydrate adding to 1-x molar nickel chloride hexa-hydrate where x = 0.02, 0.05, 0.08. [2]

To produce an Eu doped NiO sample, the green solution which is shown in

Figure 5.1: The obtained green solution.

Figure 5.1 was washed using distilled water many times until the pH value reached 7 at room temperature.To dry the wet solution, it was placed in a furnace at 100 C° for 20h.[2]

At the end, pellets were made out of the green powder obtained and calcined at $550C^{\circ}$ for 4 hours.[2]

5.2 X-Ray Diffraction

Powder X-ray Diffraction (PXRD) measurements carried out on the samples to confirm that the doping was achieved. The PXRD patterns for the pure and doped samples of nickel oxide show five dominant peaks located at $2\theta = 37.1$, 43.2, 62.8, 75.3 and 79.3(deg),

corresponding to (1 1 1), (2 0 0), (2 2 0), (3 1 1), (2 2 2) planes. No secondary peaks were detected which establishes no impurity phase in the substitution of Eu at the Ni sites, which confirms we have used an appropriate method of synthesising the samples (see Figure 5.2).

The X-ray software analysis PDXL2 was employed on the results to perform Rietveld refinement and identify the composition of the samples with access to the Inorganic Crystal Structure Database (ICSD) in addition to providing information about the grain size, lattice parameters and crystal structures. The ionic radii of the host and the dopant were not close in size for Ni^{+2} and Eu^{+3} ionic radii are $0.69A^{\circ}$ and $1.07A^{\circ}$, respectively. The crystal structure of all samples was found to be face center cubic (fcc) with Fm-3m space group as reported previously only for NiO .[24]

It has to be mentioned here that the X-ray diffractometer is not designed to detect precisely the concentration of the dopants, the lattice parameter found for pure NiO is 4.189 A° which is the same as the reported value.[2]

The Rietveld refinement parameters for all samples are tabulated in Table 5.1. In addition, using the Rigaku X-ray analysis software, the average particle size of pure NiO and the doped samples are tabulated in Table 5.2. Furthermore, by plotting the lattice parameters as a function of Eu concentration a reduction in the lattice constant with increasing Eu concentration was observed (see Figure 5.3). The results showed that as we increase the Eu concentration, the $Ni_{1-x}Eu_xO$ become more dense although the ionic radius of Eu^{3+} is larger than Ni^{2+}. The lattice parameter measurement error is about $\pm$ 0.001 A°.

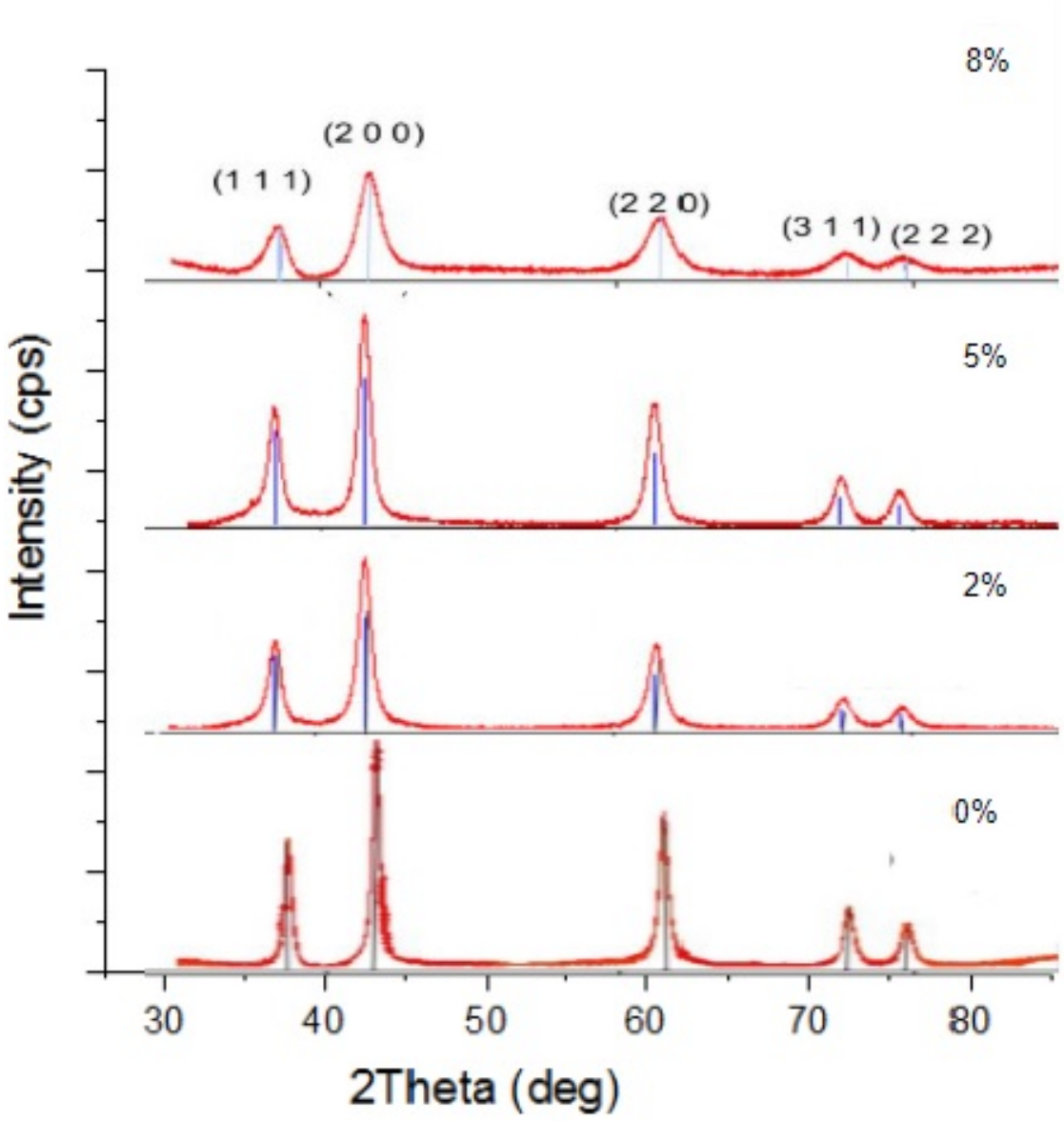

Figure 5.2: Powder X-ray diffraction pattern of the pure and Eu doped NiO nanoparticles.

Compound	R_{wp}	R_e	Chi^2
NiO	7.99	6.99	1.3302
$Ni_{0.98}Eu_{0.02}O$	1.48	0.7	4.4419
$Ni_{0.95}Eu_{0.05}O$	1.15	0.49	5.4319
$Ni_{0.92}Eu_{0.08}O$	1.83	0.62	8.6583

Table 5.1: The Rietveld refinement, which is a method of analysis to fit the experimental diffraction patterns with calculated profiles, parameters for pure and doped samples.

Compound	Average particle size	Lattice Constant
NiO	3.0 nm	4.186 $A°$
$Ni_{0.98}Eu_{0.02}O$	5.5 nm	4.179 $A°$
$Ni_{0.95}Eu_{0.05}O$	5.4 nm	4.174 $A°$
$Ni_{0.92}Eu_{0.08}O$	4.3 nm	4.168 $A°$

Table 5.2: The average particle size and the lattice parameters for each sample.

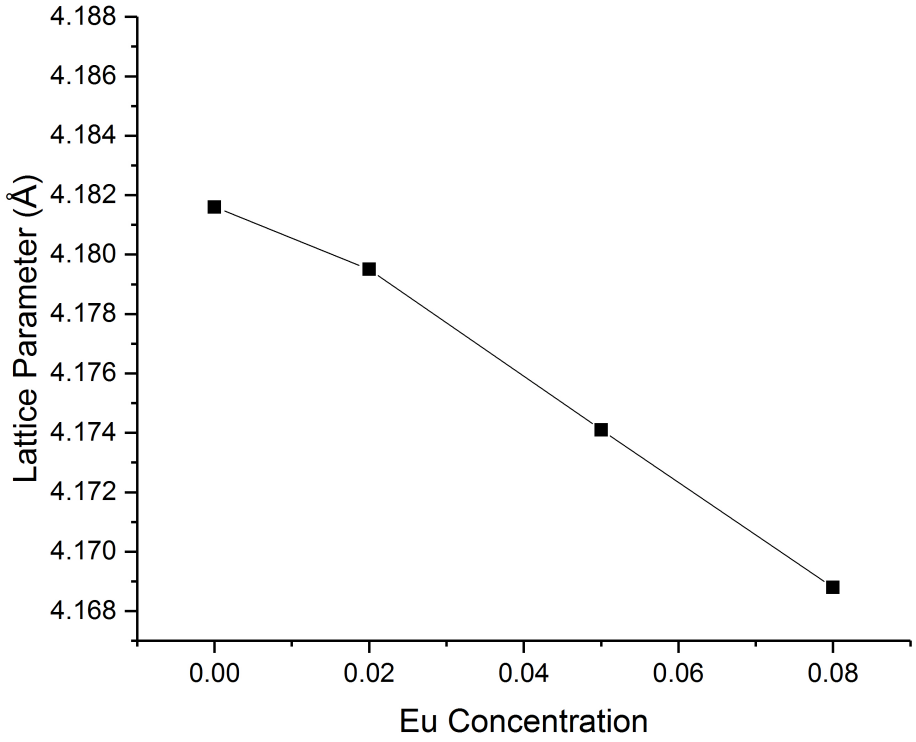

Figure 5.3: Lattice parameter as a function of Eu concentration with an error about $\pm$ 0.001 $A°$.

5.3 Electrical Resistivity

The electrical resistivity of the samples at high temperatures was carried out using the method which was discussed in chapter 2 and the results are presented in this section.

Compound	E_g below 460K	E_g above 460K
NiO	0.829 eV	0.829 eV
$Ni_{0.98}Eu_{0.02}O$	0.481 eV	0.991 eV
$Ni_{0.95}Eu_{0.05}O$	0.432 eV	0.841 eV
$Ni_{0.92}Eu_{0.08}O$	0.506 eV	0.900 eV

Table 5.3: Shows the energy gap values for each sample above and below 460 K.

Using the relation between the conductivity and the energy gap, the band gap values were obtained for pure and doped samples.

$$\sigma = \sigma(0)\exp(E_g/2K_bT) \tag{5.1}$$

where $\sigma(T)$ is the conductivity at temperature T and K_b is the Boltzmann factor. Using the relation $\rho(T) = 1/\sigma(T)$ where $\rho(T)$ is resistivity at temperature T and taking the natural logarithm the relation between $\rho(T)$ and E_g can be written as:

$$ln(\rho(T)) = -E_g/2K_bT + ln(\rho(0)) \tag{5.2}$$

Hence, as $R(T)$ is proportional to $\rho(T)$, the slope of $ln(R(T)/lnR(0))$ (R(0) is the resistance at absolute zero temperature estimated by extrapolating the R value to 0 K) versus -$1/2K_bT$ in Figure 5.4 gives the energy gap for pure and doped samples which shows a general decrease in E_g with increasing the dopant percentage.

It can also be concluded that with increasing the Eu percentage, the resisitivity plot versus temperature becomes slightly more conductive (see Figure 5.5). We observed that at 460 K the energy gap changes by a factor of 2 for the doped samples and that it became smaller below 460 K showing the samples becoming more conductive compared to pure NiO.

Table 5.3 provides the value of the energy gap above and below 460 K for

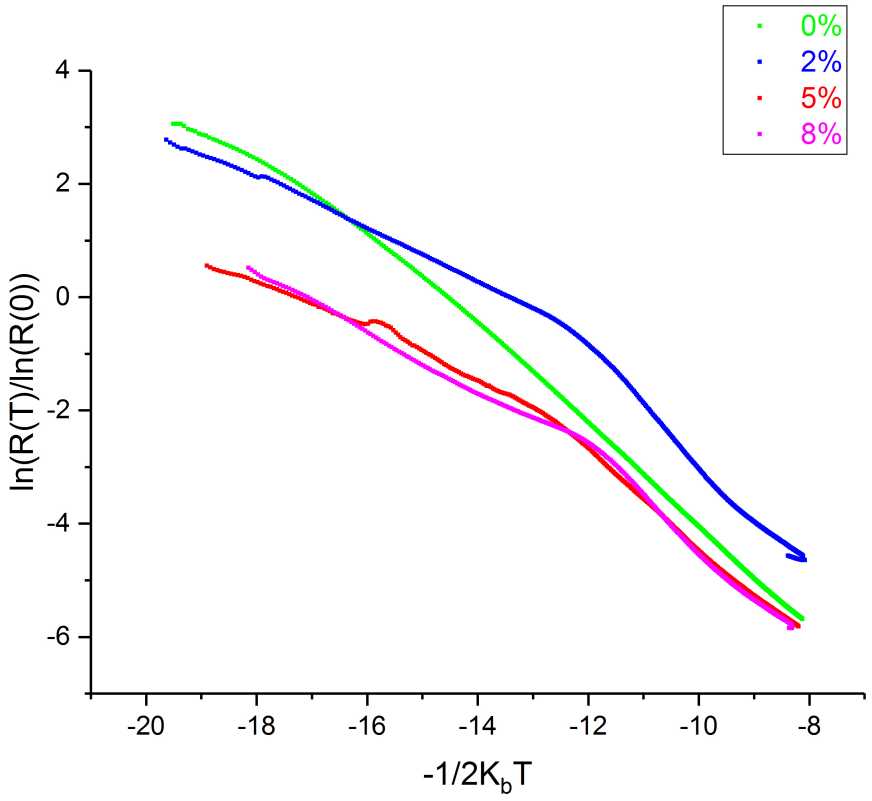

Figure 5.4: Slope shows how the energy gap changes for pure and doped samples.

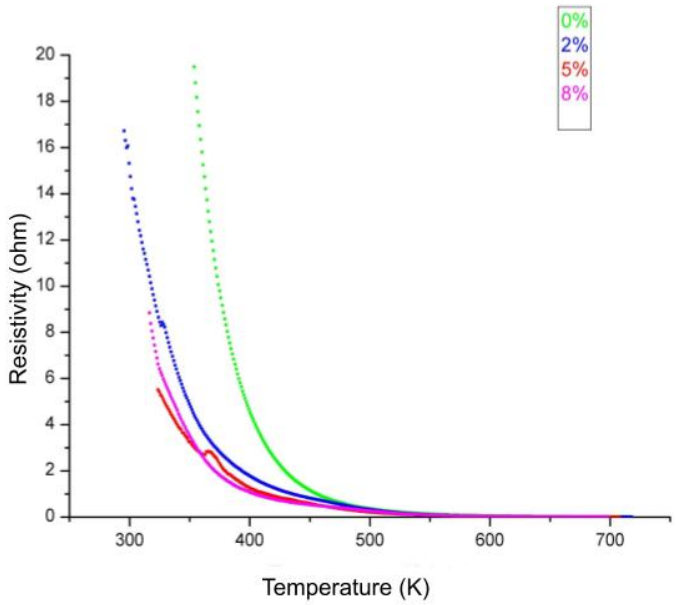

Figure 5.5: Resistivity as a function of temperature for pure and doped samples.

each sample. The energy gap in the doped samples indicates a decrease above 460 K, however, it increases as temperature goes below 460 K. Thus it can be concluded that the substitution of Eu in Ni sites, has made NiO more conductive at temperatures below 460 K. The slight changes in the resistance of the sample can be attributed to the slight movement of the sample during the experiment.

5.4 Magnetic Properties

The magnetization measurements presented in this thesis are discussed in two parts. The first part is dedicated to AC measurements which were carried out using the modulation coil. The second part discusses DC measurements which were carried out using the oven extension inserted in the Quantum Design Magnetic Properties Measurements (MPMS).

The difference between AC and DC magnetic measurements arises from the

different types of applied magnetic fields on samples. An AC magnetometer applies an AC magnetic field on samples which means it is time-dependent, while the magnetic field in DC measurements is time-independent. Thus AC susceptibility provides information about the dynamics of the magnetic moments and measures the samples' susceptibility which is equal to dM/dH. In the DC magnetometer the equilibrium value of the magnetization is obtained. Hence, the same magnetic behaviour can not be expected for identical samples which means the phase transition happens at about the same temperature as for the AC magnetometer but with a different signature.

In addition, studying of AC susceptibility is helpful for investigating on intermetallic rare earth elements and transition metals since these elements (in my case Ni and Eu) are behaving in a competition between antiferromagnetic and ferromagnetic interactions which yields a phase transition via a different magnetic order.[25]

I will start with the AC magnetization results. Different types of magnetic samples were measured. The reliability of the experiment was tested by repeating it via the DC magnetometer.

5.4.1 AC Magnetization

The AC susceptibility measurements were carried out by high temperature ac-magnetometer on $Ni_{1-x}Eu_xO$ (x= 0, 0.02, 0.05, 0.08), as well as on the pure and doped strontium hexaferrite samples of my colleague.[8] The transition temperatures for $Ni_{1-x}Eu_xO$ samples could not measure with enough resolution, however; for the test samples of strontium hexaferrite and bismuth ferrite were successfully detected and are discussed in more detail later on in this chapter. The response of the high temperature ac- magnetometer without a sample (back ground (BG)) showed a transition at 435 K. To find out the cause of this transition, some of the components of the ac-magnetometer were switched with different

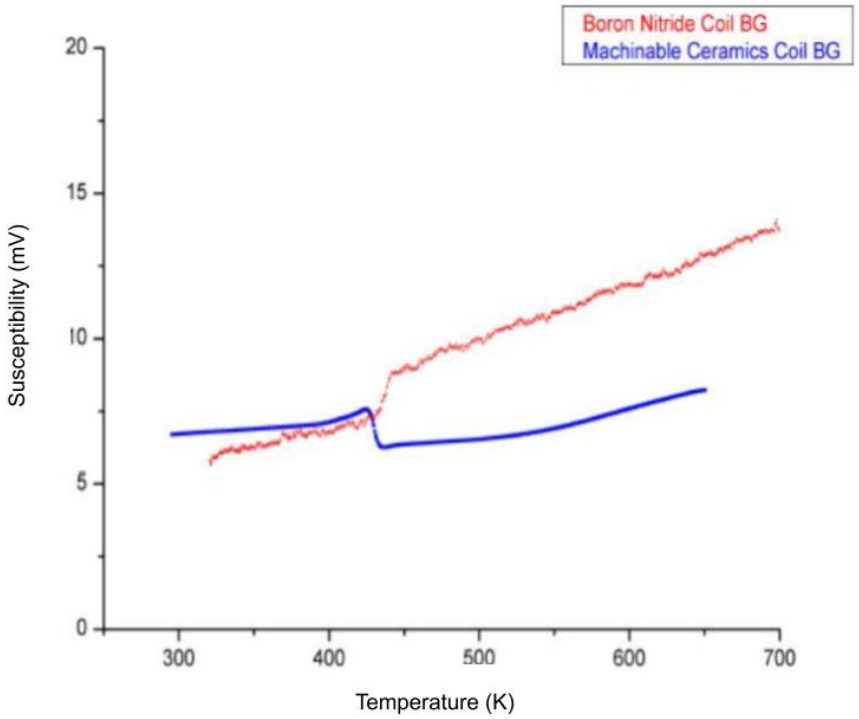

Figure 5.6: The back ground results for the machinable ceramic and boron nitride The blue graph is associated with the machinable ceramics and the red graph is related to boron nitride where both are showing a transition around 435K. the difference between the two plots is due to the slight phase shift at the start of measurements.

materials. First, the nichrome wires were replaced by copper wires, but the transition did not disappear. To solve the problem, I also replaced the machinable ceramic coil holders with boron nitride which showed the same transition at 435 K temperature (see Figure 5.5). Hence, the transition was accepted as a part of the background which was subtracted from the measurement results. All the measurements were carried out at the frequency of 517 Hz.

Machinable ceramics showed better hardness than boron nitride at high temperature. In addition, copper wires were not used as a coil because they exhibited oxidization at higher temperature, consequently nichrome wire was used.

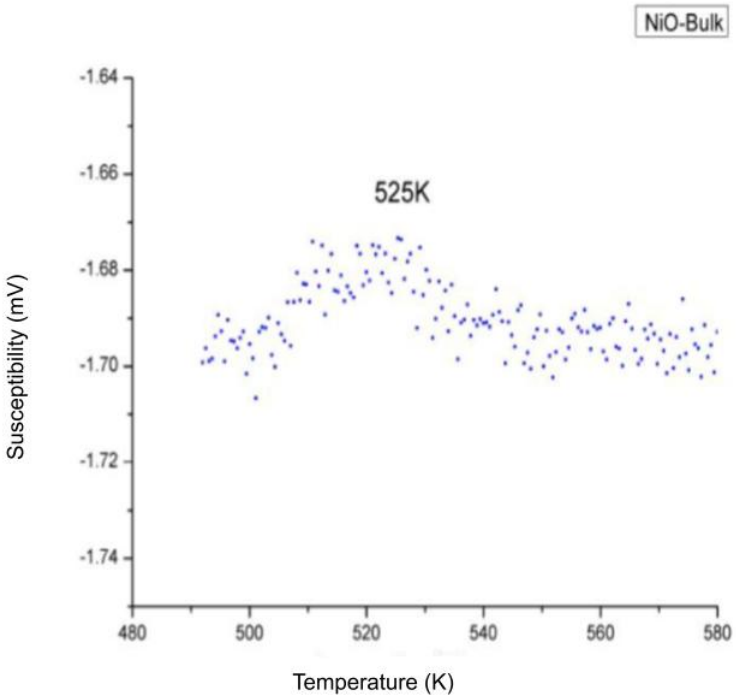

Figure 5.7: *Néel* transition in bulk NiO at 525 K. In addition, since the voltage is proportional to the susceptibility, mV was used as the unit for ac susceptibility.

The temperature-dependent susceptibility for bulk NiO is seen in Figure 5.6 that shows *Néel* temperature at 525 K which is close to the reported value, 523 K.[2]

The Curie temperature reported for strontium hexaferrite is 737 K which occurs at high temperatures and suitable to be investigated on with the oven. The Curie transition was detected with the ac-magnetometer at the same temperature as for the temperature reported in publication which can be seen in Figure 5.7.[26] The strontium hexaferrite samples which were studied in this thesis are magnetic semiconductors ceramics nano-particles which shows intriguing properties than that of the bulk strontium hexaferrite samples counterpart and have a wide range of applications from permanent magnetic materials to microwave devices.[27][28]

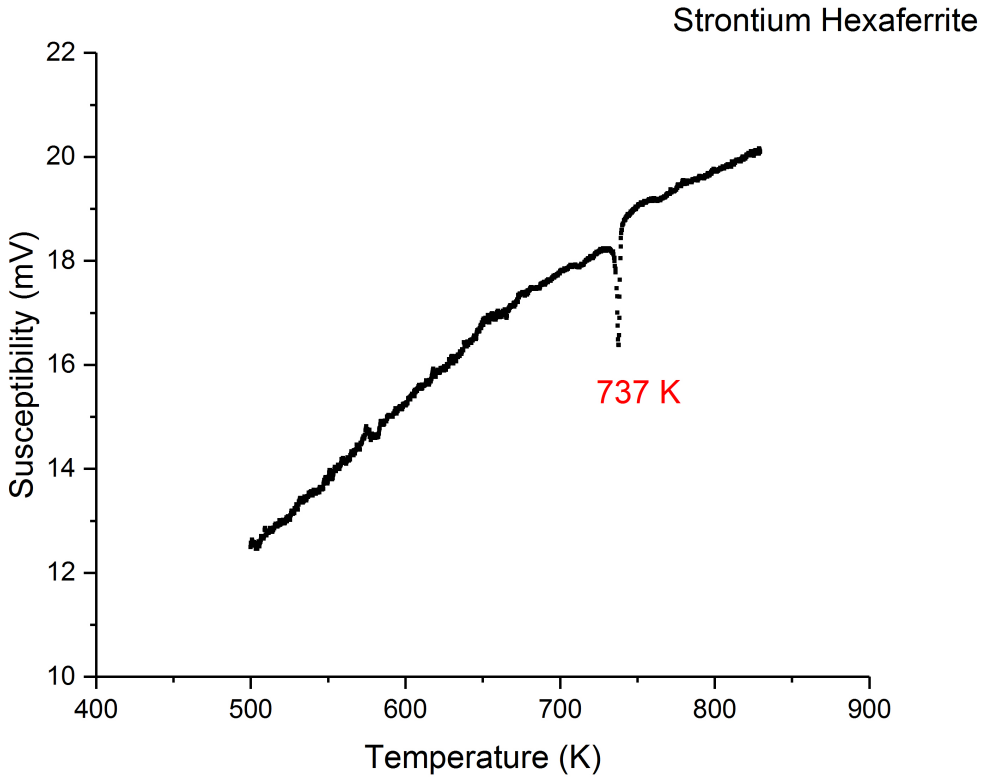

Figure 5.8: The Curie temperature of the pure strontium hexaferrite was detected using the ac-magnetometer measurement at 737 K.

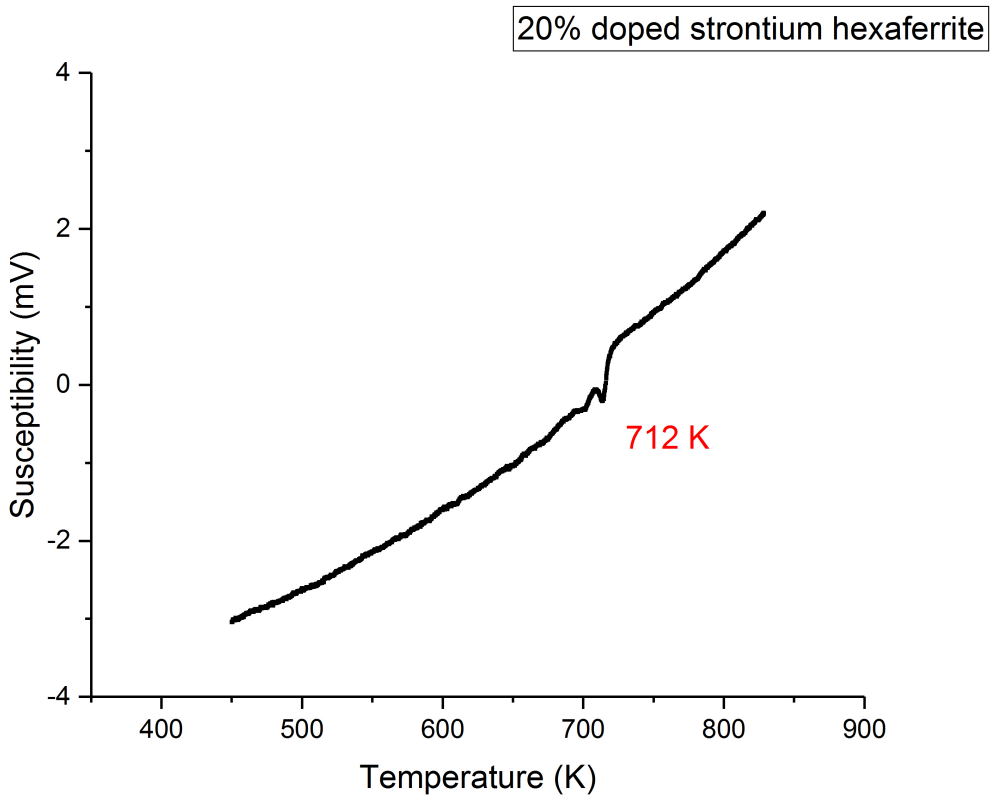

Figure 5.9: The Curie temperature for 20% doped strontium hexaferrite occurs at 712 K.

Figure 5.8 and Figure 5.9 represent the susceptibility versus temperature for 20% and 40% doped samples of strontium hexaferrite as a function of Co substitution for Fe, the transition temperatures were detected at 712 K and 693 K, respectively which shows the reduction in the ferromagnetic transition temperature by increasing the dopant.

In addition, bismuth ferrite with antiferromagnetic properties, another of my colleague's samples, was tested using the high temperature ac coil. The antiferromagnetic transition temperature was observed at 636 K Figure 5.10, similar to the reported value of 643 K.[29]

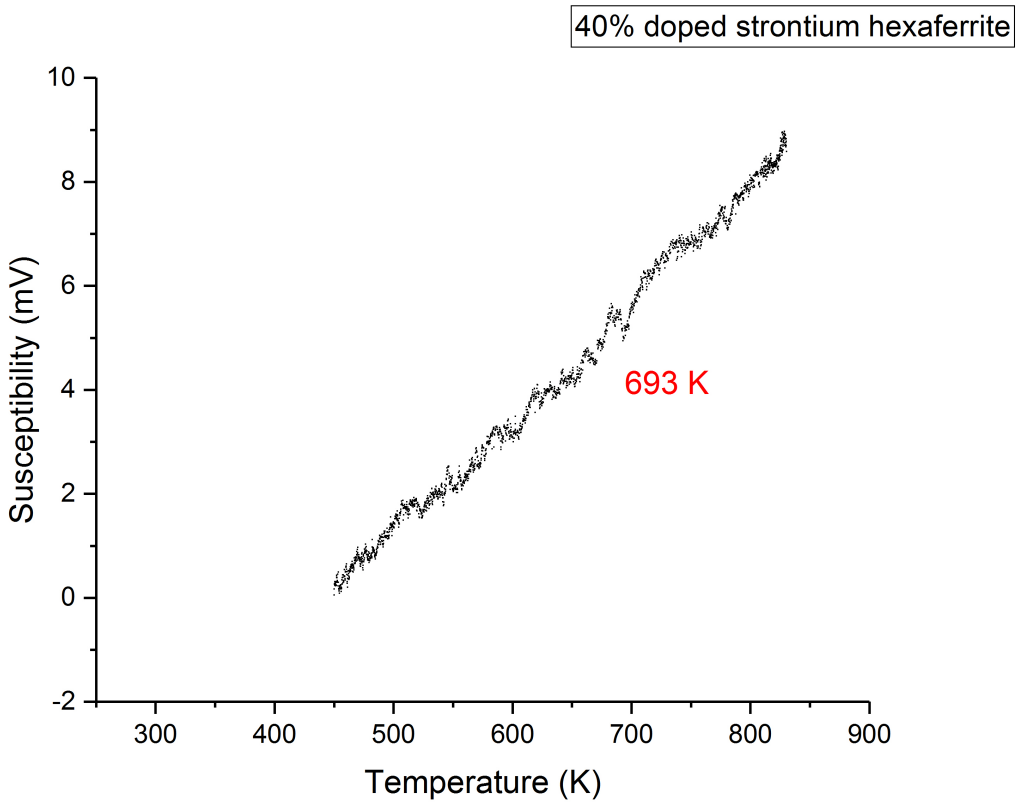

Figure 5.10: The temperature dependence ac susceptibility for 40% doped strontium hexaferrite is illustrated.

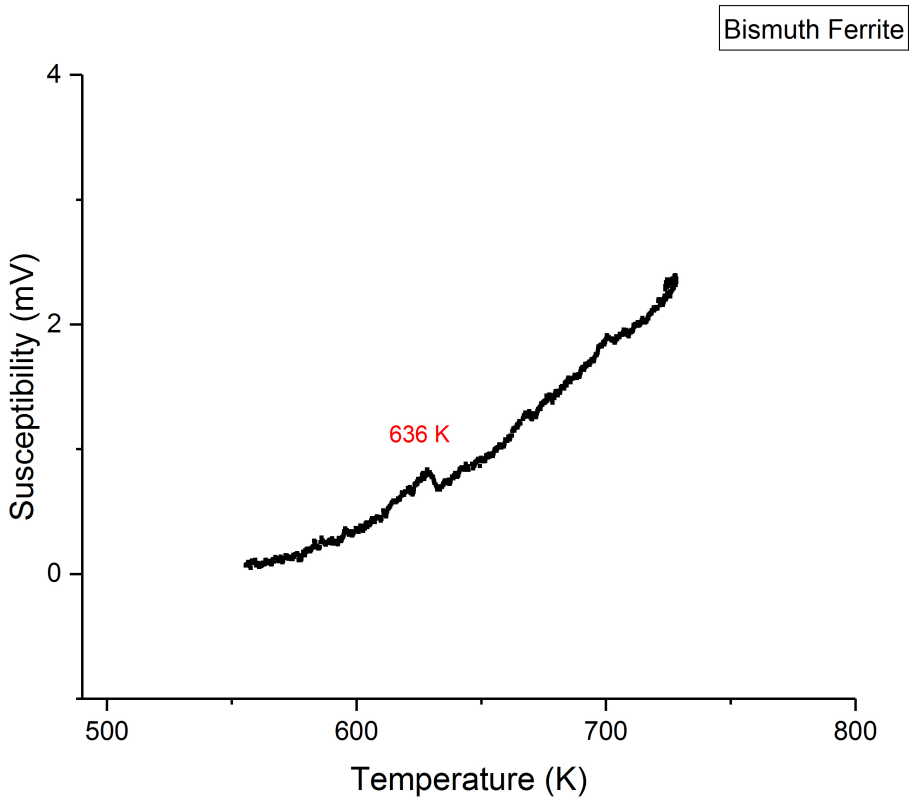

Figure 5.11: The temperature dependence of the relative susceptibility of bismuth ferrite showing the antiferromagnetic transition at 636 K.

5.4.2 DC Magnetization

To test the new oven for the SQUID magnetometer, the temperature dependence of the DC magnetization of all samples was measured in a temperature range from 400 K to 750 K. The magnetization measurements for all samples of strontium 100 Oe. However, the signal from NiO samples were low due to the less amount of mass and the transitions couldn't be detected.

The magnetic response of the brass sample holder (BG) was measured and fitted to a polynomial degree of three. Then, based on the temperatures at which the magnetic moment of the samples was measured, the BG was calculated using the polynomial

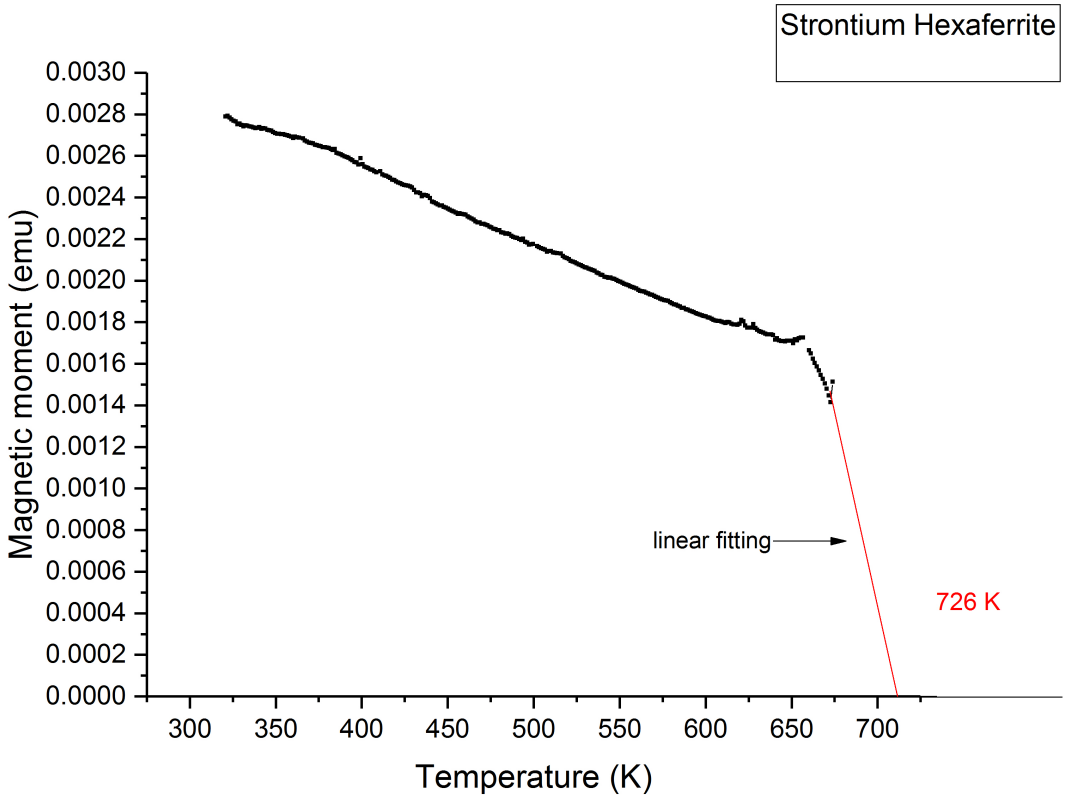

Figure 5.12: The magnetization of strontium hexaferrite decreases with increasing the temperature.

function and subtracted from the measured magnetic moment data to obtain the magnetic moment of the sample. The same samples were used to check the reliability of the oven for the SQUID magnetometer by comparing the transition observed using dc-measurements to that of the results from the high temperature ac-magnetometer.

The magnetization of strontium hexaferrite shows a reduction with increasing the temperature. Due to the overheating of the magnetometer as a result of the oven radiation, the measurement was carried out to about 700 K. At 670 K, a sharp reduction of the susceptibility was observed. The experiment had to be stopped at 675 K to prevent any overheating of the SQUID magnetometer. It can be seen that the sample magnetic moment approaches a value close to zero at the so-called Curie temperature, about 726

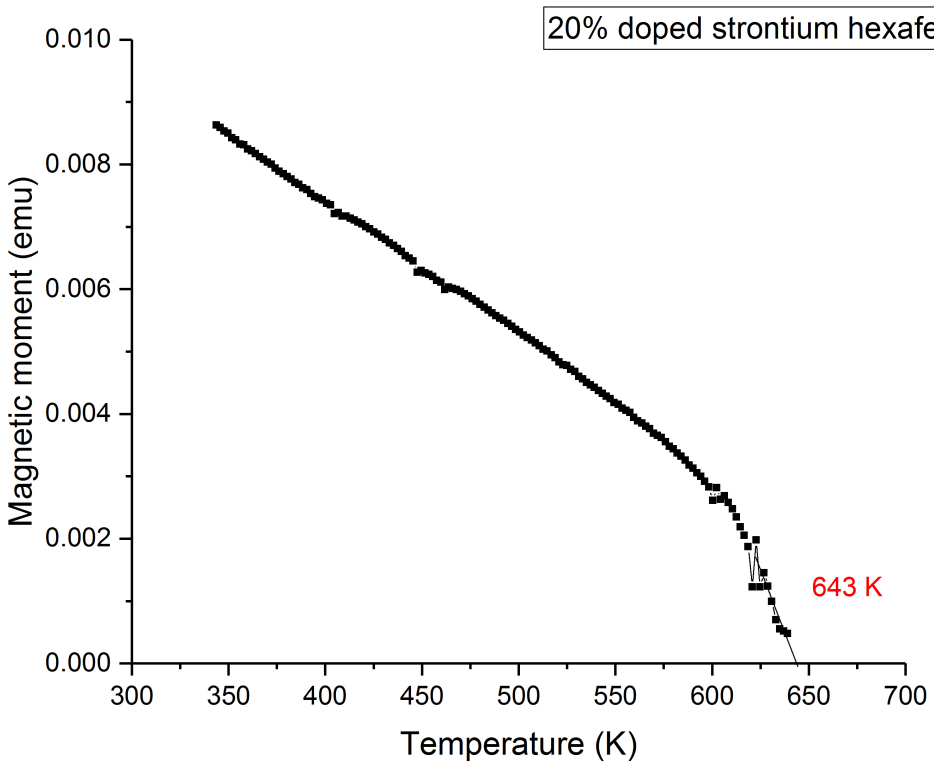

Figure 5.13: Magnetization of 20% doped strontium hexaferrite as a function of temperature.

K corresponding to the ferromagnetic transition of strontium hexaferrite (see Figure 5.11). This transition temperature is lower than the T_C observed via high temperature ac-magnetization at 737 K, which is an indication that our calibration of the new oven for the SQUID magnetometer is off by about 11 K.

The magnetization of 20% doped strontium hexaferrite shows the Curie temperature at 643 K while for 40% doped strontium hexaferrite, the Curie temperature happens at 619K (see Figure 5.12 and Figure 5.13). It is thus concluded that there is a reduction in the Curie temperature by increasing the dopant percentage.

The DC measurement was also carried out on bismuth ferrite in a 5000 Oe DC magnetic field. For bismuth ferrite, the transition from antiferromagnetic to paramag-

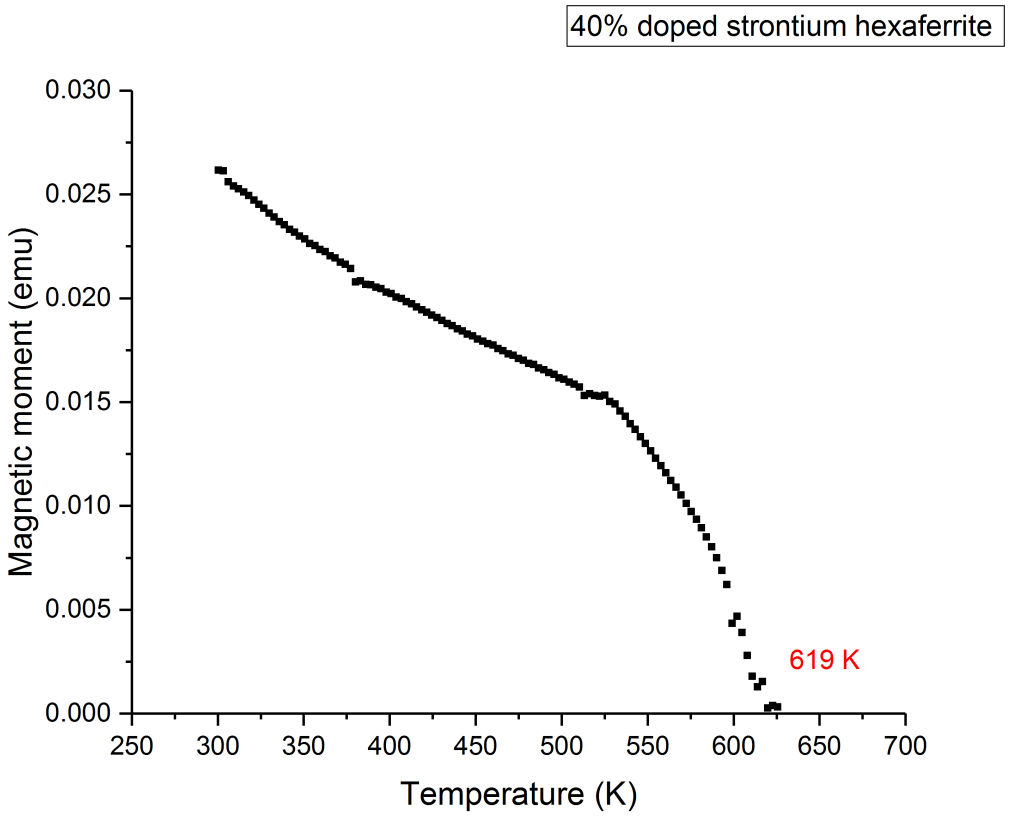

Figure 5.14: Magnetization of 40% doped strontium hexaferrite as a function of temperature.

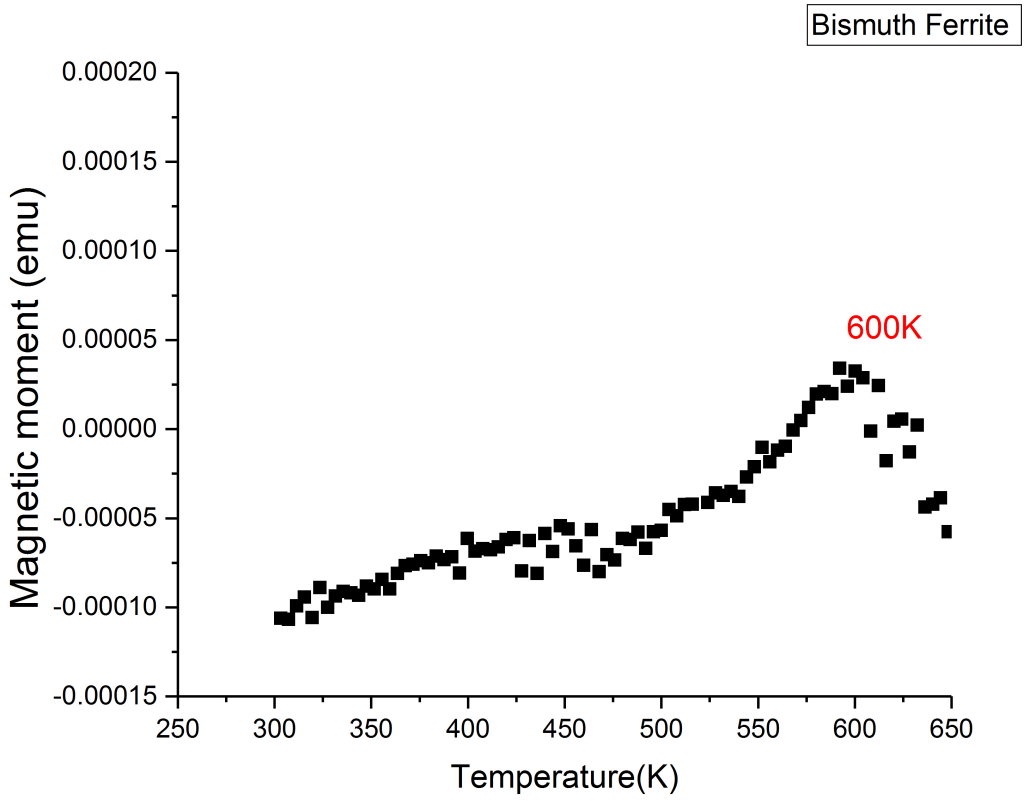

Figure 5.15: The antiferromagnetic transition at 600K for bismuth ferrite.

netic order was detected at 600K (see Figure 5.14).

A comparison between the transition temperatures measured for the hexaferrite test samples using the SQUID magnetometer in the oven designed and the high temperature ac-magnetization are provided in Table 5.4. As can be seen from this table, the transition temperatures measured using the designed oven for the SQUID magnetometer differ from that of the ac-magnetization measurement. The results obtained using the ac-magnetization is accurate within ± 2 K as we used a commercial calibrated temperature probe. There are several factors causing the inaccuracy in temperature measurements in the oven designed for the SQUID magnetometer. In the design of the oven for the SQUID magnetometer, we should decrease the length of the oven by about 40%-50% in order to reduce the radiation, which causes a rapid heating of the oven as well as high

Sample	AC	DC	Reported Value
Strontium hexaferrite	737 K	725 K	737 K [26]
20% doped strontium hexaferrite	712 K	643 K	NA
40% doped strontium hexaferrite	693 K	619 K	NA
Bismuth Ferrite	636 K	600 K	643 K [29]

Table 5.4: Comparison of the obtained and reported values of the test samples by both methods.

radiation heating absorbed by the SQUID magnetometer itself. The oven for the SQUID magnetometer needs to be re-calibrated precisely. At present, the thermometer is 100 mm away from the center of the oven. This distance needs to be reduced.

This should be done by calibrating the oven thermometer relative to the position of the sample during the measurement as closely as possible. This can be done by reducing the length of the oven by half which would not only allow a better reading of the sample temperature, but would also reduce the radiation heat to the SQUID magnetometer.

Chapter 6

Conclusions

Nano-particle (NP) samples of pure and Eu doped NiO were synthesized successfully via a co-precipitation method. The structure of the samples was confirmed via X-ray diffraction to be a face centered cubic. These samples were semiconductors and their energy gap was reduced as a function of increasing concentration of Eu.

An oven was designed to provide an increased range for measuring the temperature range of the SQUID magnetometer from 400 K maximum to 800 K. To confirm that this oven works with the SQUID magnetometer, we checked the susceptibility and the magnetic phase transition of known samples. Furthermore, we also measured the magnetic properties of these samples by designing an ac-magnetometer which can be inserted into a commercial oven capable of reaching 1100 K. The ferromagnetic phase transition temperature of hexaferrite and the antiferromagnetic *Néel* temperature of bismuth ferrite were investigated by both systems.

Although the oven measured the magnetic properties of the samples up to 750 K, there is still more work to be done on the oven in order to improve the quality of the measurement including a better calibration of the oven. The measurement results obtained from the dc SQUID magnetometer showed the transition temperatures for the hexaferrite samples occurring at lower temperatures compared to accepted results and literature from the ac-magnetometer measurements.

Furthermore, at higher temperature above 650 K the system needs to be remotely monitored to prevent overheating of the SQUID magnetometer system. This can be solved by reducing the radiation heating of the magnetometer by the oven at temperatures above 650 K. The measuring thermometer needs to be installed closer to the center of the magnetometer. This can be achieved by reducing the length of the oven by a factor of 40 to 50%.

The present design showed that the oven does not generate any magnetic noise caused by the current through the heater that out prevent the SQUID magnetometer from measuring the magnetic moment of a small sample. Using this oven prototype we are able to construct a new oven that allows the user to measure a sample at temperatures as high as 800 K.

Bibliography

[1] M.W. Vernon and M.C. Lovell. Anomalies in the electrical conductivity of nickel oxide above room temperature. *Journal of Physics and Chemistry of Solids*, 27(6):1125–1131, 1966.

[2] J Al Boukhari, L Zeidan, A Khalaf, and R Awad. Synthesis, characterization, optical and magnetic properties of pure and Mn, Fe and Zn doped NiO nanoparticles. *Chemical Physics*, 516:116–124, 2019.

[3] Hong Jian Zhao, Wei Ren, Xiang Ming Chen, and L Bellaiche. Effect of chemical pressure, misfit strain and hydrostatic pressure on structural and magnetic behaviors of rare-earth orthochromates. *Journal of Physics: Condensed Matter*, 25(38):385604, aug 2013.

[4] Marin Tadic, Dobrica Nikolic, Matjaz Panjan, and Graeme R Blake. Magnetic properties of nio (nickel oxide) nanoparticles: blocking temperature and neel temperature. *Journal of Alloys and Compounds*, 647:1061–1068, 2015.

[5] Fan H. Wang N. et al Sun, J. Mfluorescent vancomycin and terephthalate comodified europium-doped layered double hydroxides nanoparticles: synthesis and application for bacteria labelling. *Jornal of Nanoparticle Research*, 16, 2014.

[6] Vikas Dubey, Jagjeet Kaur, and Sadhana Agrawal. Effect of europium doping levels on photoluminescence and thermoluminescence of strontium yttrium oxide phosphor. *Materials Science in Semiconductor Processing*, 31:27 – 37, 2015.

[7] G.J. [Barbosa Junior], A.M. Sousa, S.M. [de Freitas], R.D.S. Santos, and M.V.dos S. Rezende. Investigation of europium dopant in the orthophosphate kmpo4 (m = ba and sr) compounds. *Journal of Physics and Chemistry of Solids*, 130:282 – 289, 2019.

[8] Sara Hatefi Monfared. Private discussion. *Brock press*, 2020.

[9] Charles Kittel. *Introduction to solid state physics*. Wiley, New York, 7th ed. edition, 1996.

[10] Fereidoon S. Razavi. Personal conversation, March 2019.

[11] Nicola A. Spaldin. *COMBINATION OF FIRST-PRINCIPLES & SEMI-EMPIRICAL TECHNIQUES*. Cambridge, 2018.

[12] J. M. D. Coey. *Magnetism and magnetic materials*. Cambridge University Press, 2010.

[13] N. W. Ashcroft and N. D. Mermin. *Solid State Physics*. Holt-Saunders, 1976.

[14] Quantum Design, 11578 Sorrento Valley Rd San Diego USA. *Physical Property measurement system*, 1999.

[15] Mathew Pula. Investigation into the magnetoelectric effect and magnetic properties of iron-doped cobalt molybdate. Master's thesis, Brock University, 2019.

[16] Inc Quantum Design. magnetic property measurement system, 2016.

[17] LH Lewis and Konrad M Bussmann. A sample holder design and calibration technique for the quantum design magnetic properties measurement system superconducting quantum interference device magnetometer. *Review of scientific instruments*, 67(10):3537–3542, 1996.

[18] S Bedanta, O Petracic, M Aderholz, and W Kleemann. A sample holder design for high temperature measurements in superconducting quantum interference device magnetometers. *Review of scientific instruments*, 76(8):083910, 2005.

[19] G. ERHARD. Melting-points of commercial brasses and bronzes. *Journal of the Franklin Institute*, 177(4):463, 1914.

[20] Hadi Tavakkoli, Ebrahim Abbaspour-Sani, Amin Khalilzadegan, Amir-Musa Abazari, and Ghader Rezazadeh. Mutual inductance calculation between two coaxial planar spiral coils with an arbitrary number of sides. *Microelectronics Journal*, 85:98–108, 2019.

[21] Clayton R Paul. *Inductance: loop and partial*. John Wiley & Sons, 2011.

[22] MSc Renneboog, Richard M. Faraday's law. *Salem Press Encyclopedia of Science*, 2019.

[23] A.S. Morris and R. Langari. *Measurement and Instrumentation: Theory and Application*. Elsevier Science, 2015.

[24] Kiran N. Patel, M.P. Deshpande, Krishna Chauhan, Piyush Rajput, Vivek P. Gujarati, Swati Pandya, Vasant Sathe, and S.H. Chaki. Effect of mn doping concentration on structural, vibrational and magnetic properties of nio nanoparticles. *Advanced Powder Technology*, 29(10):2394 – 2403, 2018.

[25] M Balanda. Ac susceptibility studies of phase transitions and magnetic relaxation: conventional, molecular and low-dimensional magnets. *Acta Phys. Pol. A*, 124(6):964–976, 2013.

[26] Z.F. Zi, Y.P. Sun, X.B. Zhu, Z.R. Yang, J.M. dai, and W.H. Song. Structural and magnetic properties of srfe12o19 hexaferrite synthesized by a modified chemical co-

precipitation method. *Journal of Magnetism and Magnetic Materials*, 320(21):2746–2751, 2008.

[27] M.A. Almessiere, Y. Slimani, and A. Baykal. Structural and magnetic properties of ce-doped strontium hexaferrite. *Ceramics International*, 44(8):9000 – 9008, 2018.

[28] H.Z. Wang, B. Yao, Y. Xu, Q. He, G.H. Wen, S.W. Long, J. Fan, G.D. Li, L. Shan, B. Liu, L.N. Jiang, and L.L. Gao. Improvement of the coercivity of strontium hexaferrite induced by substitution of al3+ ions for fe3+ ions. *Journal of Alloys and Compounds*, 537:43 – 49, 2012.

[29] A.K. Zvezdin, A.M. Kadomtseva, S.S. Krotov, A.P. Pyatakov, Yu.F. Popov, and G.P. Vorobyev. Magnetoelectric interaction and magnetic field control of electric polarization in multiferroics. *Journal of Magnetism and Magnetic Materials*, 300(1):224–228, 2006. The third Moscow International Symposium on Magnetism 2005.